Supporting Information

First tetrametallic 19-nuclear Ce^{III}–Sc^{III}–W^{VI}–Sb^{III} cluster-incorporated polyoxometalate for electrochemical biosensing of CYFRA21-1

Jiaxin Li, Zhigang Tang, Yu Liu,* Lijuan Chen* and Junwei Zhao*

Henan Key Laboratory of Polyoxometalate Chemistry, College of Chemistry and Molecular Sciences, Henan University, Kaifeng 475004, People's Republic of China.

E-mail: 986367749@qq.com, ljchen@henu.edu.cn, zhaojunwei@henu.edu.cn

Fig. S1 The IR spectrum of **1**.

Fig. S2 Comparisons of experimental PXRD and the corresponding simulated XRD patterns of **1**.

Fig. S3 The TG curve of **1**.

Fig. S4 (a) The 2-D layered **1** viewed along the *b*-axis. (b) The 2-D layered **1** viewed along the *c*-axis.

Fig. S5 (a) Structure of polyanion **1a** viewed along the *a*-axis. (b) Structure of polyanion **1a** viewed along the *b*-axis. (c) Structure of polyanion **1a** viewed along the *c*-axis.

Fig. S6 The hexacoordinate Sc^{3+} cations serve as the symmetry center of **1a** to form two identical **1b**.

Fig. S7 The nine-coordinate monocapped square antiprismatic configuration of $Ce1^{3+}$ cation.

Fig. S8 Each of a Ce^{3+} and a Sb^{3+} cation is capped onto the octahedral $[Sc_2W_5O_{13}]^{10+}$ cluster through two oxygen atoms.

Fig. S9 (a) The vacancies in the three [B-*β*-SbW_9O_{33}]$^{9-}$ BBs in **1b** contain twenty-one highly reactive terminal oxygen sites. (b) The $W1^{VI}$, $W4^{VI}$ and $W8^{VI}$ centers each occupy two exposed sites of one [B-*β*-SbW_9O_{33}]$^{9-}$ BBs. (c) The $W32^{VI}$, $Sc2^{3+}$ and $Sc3^{3+}$ cations occupy 12 exposed sites of the three [B-*β*-SbW_9O_{33}]$^{9-}$ BBs. (d) The $Ce1^{3+}$ center occupies one exposed site of each [B-*β*-SbW_9O_{33}]$^{9-}$ BB.

Fig. S10 These two triangular planes composed of W^{VI} centers and Sc^{3+} cations are staggered at an angle of 60°.

Fig. S11 (a) The chair-like conformation of **1a**. (b) The chair-like conformation of $[(B\text{-}\beta\text{-}SbW_9O_{33})_4(B\text{-}\alpha\text{-}SbW_9O_{33})_2(WO_2)_4(WO(H_2O))_6WO_5(H_2O)]^{26-}$. (c) The chair-like conformation of $[Fe_{11}(H_2O)_{14}(OH)_2(W_3O_{10})_2(B\text{-}\alpha\text{-}SbW_9O_{33})_6]^{27-}$. (d) The chair-like conformation of $[Sc_{11}W_6O_{20}(OH)_2(H_2O)_{16}(B\text{-}\beta\text{-}SbW_9O_{33})_6]^{27-}$. (e) The chair-like conformation of $[Sc_7Sb_2W_6O_{20}(H_2O)_8(B\text{-}\beta\text{-}SbW_9O_{33})_6]^{31-}$.

Fig. S12 IR spectra of **1–Cs** obtained from the aqueous solution of **1** by re-precipitating **1** with using CsCl.

Fig. S13 (a) DPV curves and (b) I_{Fe} signal variations of different electropolymerization voltages (0.65, 0.75, 0.80 and 0.85 V). **1**: 50 mg·mL^{-1}, PY: 5 mM, and electropolymerization time: 50 s.

Fig. S14 (a) DPV curves and (b) I_{Fe} signal variations of different electropolymerization times (20, 30, 40, 50, 60 and 70 s).

Fig. S15 (a) SEM image of **1**@PPY film. (b–g) SEM elemental mapping images of the **1**@PPY film with C, N, W, Sc, Ce, and Sb elements. (h) The SEM elemental mapping profile of the **1**@PPY film.

Fig. S16 The cross-sectional thickness of the **1**@PPY film (**1**: 50 mg·mL^{-1}, PY: 5 mM, electropolymerization voltage: 0.8 V, and electropolymerization time: 50 s).

Fig. S17 EIS responses of the **1**@PPY/GCE and bare GCE.

Fig. S18 (a) The SEM image of Au/**1**@PPY. (b–h) The SEM elemental mapping images of the Au/**1**@PPY film, corresponding to Au, W, C, N, Sb, Ce and Sc elements, respectively. (i) The SEM elemental mapping profile of the Au/**1**@PPY film.

Fig. S19 (a) DPV current values (I_{Fe}) of the **1**-ECBS detecting CYFRA21-1 (10^{-10} M) co-existing with interfering DNA substances (10^{-9} M). (b) DPV current values (I_{Fe}) of the **1**-ECBS detecting CYFRA21-1 (10^{-10} M) co-existing with interfering DNA substances (10^{-8} M). (c) DPV current values (I_{Fe}) of the **1**-ECBS detecting CYFRA21-1 (10^{-10} M) co-existing with interfering DNA substances (10^{-7} M). a: CYFRA21-1, b: CYFRA21-1 + 1-mis-DNA, c: CYFRA21-1 + 2-mis-DNA, d: CYFRA21-1 + 3-mis-DNA, e: CYFRA21-1 + non-DNA, f: CYFRA21-1 + 1-mis-DNA + 2-mis-DNA, g: CYFRA21-1 + 1-mis-DNA + 3-mis-DNA, h: CYFRA21-1 + 1-mis-DNA + non-DNA, i: CYFRA21-1 + 2-mis-DNA + 3-mis-DNA, j: CYFRA21-1 + 2-mis-DNA + non-

DNA, k: CYFRA21-1 + 3-mis-DNA + non-DNA, l: CYFRA21-1 + 1-mis-DNA + 2-mis-DNA + 3-mis-DNA, m: CYFRA21-1 + 1-mis-DNA + 2-mis-DNA + non-DNA; n: CYFRA21-1 + 2-mis-DNA + 3-mis-DNA + non-DNA; o: CYFRA21-1 + 1-mis-DNA + 2-mis-DNA + 3-mis-DNA + non-DNA.

Table S1. Crystallographic data and structure refinements for **1**.

Table S2. Comparison of anodic peak current and electroactive surface area between **1**@PPY/GCE and GCE.

Table S3. Comparison of the sensitivity of different electrochemical sensors for monitoring tumor markers.

Materials and physical measurements

$Na_9[B\text{-}\alpha\text{-}SbW_9O_{33}]\cdot 19.5H_2O$ was synthesized according to the previous reference.[1] All chemicals and reagents are commercially available and used without further purification. C, H, N elemental analyses were measured on a CHNS/O Vario EL Cube analyzer. The thermogravimetric (TG) analysis was carried out on the Mettler Toledo thermal gravimetric analyzer TGA/DSC 3+ under N_2 atmosphere with temperature ranging from room temperature (about 25 °C) to 1000 °C (heating rate: 10 °C·min^{-1}). Infrared spectra (400–4000 cm^{-1}) were collected by a solid sample palletized with KBr on a Bruker VERTEX 70 Fourier transform infrared spectrometer. Powder X-ray diffraction (PXRD) patterns were taken by a Bruker D8 ADVANCE apparatus with Cu Kα radiation (λ = 1.54056 Å) with a scan range (2ϑ) of 5–50° at 293 K. Scanning electron microscopy (SEM) images were obtained on a Carl Zeiss Gemini 500 field-emission scanning electron microscope equipped with energy-dispersive spectrometer (EDS). All electrochemical measurements, including cyclic voltammetry (CV), differential pulse voltammetry (DPV) and were electrochemical impedance spectroscopy (EIS) performed on a CHI660E electrochemical workstation (Shanghai Chenhua Instruments, China) at room temperature. A conventional three-electrode cell was used in all experiments, in which a modified glassy carbon electrode (GCE), a KCl–saturated Ag/AgCl electrode, and a platinum wire served as a working electrode, reference electrode, and counter electrode, respectively.

Synthesis of 1

$Na_9[B\text{-}\alpha\text{-}SbW_9O_{33}]\cdot 19.5H_2O$ (1.000 g, 0.525 mmol), $ScCl_3\cdot 6H_2O$ (0.1 g, 0.385 mmol) and dimethylamine hydrochloride (1.750 g, 21.472 mmol) were dissolved in 20.00 ml of distilled CH_3COOH–CH_3COONa buffer solution (1.50 M, pH = 5.50) upon stirring for 20min. Then, the solution was heated at 40 °C water bath for 20 min. Next, a solution of $Ce(NO_3)_3\cdot 6H_2O$ (0.250 g, 0.576 mmol) was added under stirring. The pH was adjusted to 1.50 by HCl (6.0 M). After stirring for about 30 min, the mixture was heated at 90 °C for 4.0 h (pH = 1.56), cooled to room temperature, filtered and left to evaporate for crystallization. Slow evaporation of the solution resulted in yellow rod-like crystals after several days. Yield: 16.34% based on $Ce(NO_3)_3\cdot 6H_2O$. Elemental analysis (%): C, 1.31 (calcd. 1.22); H, 1.68 (calcd. 1.55); N, 0.79 (calcd. 0.71); W, 59.28 (calcd. 59.79); Sc, 1.23 (calcd. 1.14); Ce, 2.77 (calcd. 2.85).

Preparations of buffer solution used for electrochemical measurements

Phosphate buffer solutions (PBS) (pH = 7.40) were prepared by mixing the stock solution of 100 mM NaH_2PO_4 and 100 mM Na_2HPO_4, and the pH was adjusted by using NaOH or HCl. The Fe–PBS solution (pH = 7.40) was prepared by mixing the stock solution of 100 mM phosphate buffer solutions (pH = 7.40) containing 10.0 mM $[Fe(CN)_6]^{3/4-}$. Tris-ethylenediaminetetraacetic acid buffer (TE buffer, 0.1 M, pH = 8.00) was purchased from Shanghai Sangon Biological Engineering Technological Co. Ltd. (China). The sequence of cytokeratin fragment antigen 21-1 (CYFRA21-1) and capture DNA (cDNA), 1-base mismatched DNA (1-mis-DNA), 2-base mismatched DNA (2-mis-DNA), 3-base mismatched DNA (3-mi-DNA), and non-complementary DNA (non-DNA) are similar to ctDNA were bought from Shanghai Sangon Biological Engineering Technological Co. Ltd. (China) with the following sequences:

CYFRA21-1: 5′-CGCCCCTGACACCATTCCTCCCTTC-3′

cDNA: 5′-SH-GAAGGGAGGAATGGTGTCAGGGGCG-3′

1-mis-DNA: 5′-CGCCACTGACACCATTCCTCCCTTC-3′

2-mis-DNA: 5′-CGCCCCTGACACTATTCCTCCCTTC-3′

3-mis-DNA: 5′-CGCGCATGACTCCATTCCTCTCATC-3′

non-DNA: 5′-TTGTCCAGGTAGGAGGCCAGGCGGT-3′

All the DNA were dissolved in TE buffer.

Preparation and characterization of the 1@PPY film on GCE or ITO

Electrochemical polymerization of the **1**@PPY film on GCE (**1**–PPY/GCE) or indium tin oxide (ITO) was achieved by the chronoamperometric technique in a solution containing **1** (50 mg·mL^{-1}) and 5 mM PY with a 0.8 V applied potential (*vs* Ag/AgCl). SEM was carried out with ITO as the substrate for the **1**@PPY film. The IR of **1**, PY and **1**@PPY film were tested and analyzed. The CV, DPV and EIS measurements of **1**@PPY/GCE and bare GCE were performed in Fe–PBS solution at room temperature. The electrochemical studies were all carried out on a CHI660E electrochemical workstation (Shanghai Chenhua Instruments, China).

Establishment of 1@PPY film based electrochemical biosensor[2]

(i) The GCE surface was artificially polished to a mirror-like surface using 0.05 μm alumina power on a clean gauze and cleaned with ethanol and water. Then the polished GCE was placed in the solution containing **1** and PY to prepare **1**@PPY film on GCE surface by electrochemical polymerization using the traditional three-electrode system (named **1**@PPY/GCE).

(ii) The optimization of electrodeposition time of Au NPs: The **1**@PPY/GCE was electrodeposited in 0.1 wt% $HAuCl_4{\cdot}3H_2O$ solution including 0.1 M KNO_3 under a fixed potential of −0.2 V from 30 to 80 s (*t* = 30, 40, 50, 60, 70 and 80 s); in this electrodeposition step, Au NPs were electrodeposited on the electrodes to form Au/**1**@PPY/GCE.

(iii) The optimization of incubation time between cDNA and Au NPs: 10 μL cDNA (1×10^{-6} M) was immobilized onto the Au/**1**@PPY/GCE surface via strong Au–S interactions (named cDNA/Au/**1**@PPY/GCE). The incubation time is 0, 0.5, 1, 2, 3, 4 and 5 h, respectively.

(iv) 8 μL of 6-mercapto-1-hexanol (6-MH, 1.0 mM) was covered on the surface of cDNA/Au/**1**@PPY/GCE, which was kept at room temperature for 40 min (6-MH-treated cDNA/Au/**1**@PPY/GCE) for blocking the residual Au NPs active sites.

(v) 10 μL testing solutions containing various concentrations of CYFRA21-1 ($C_{CYFRA21\text{-}1}$ = 10^{-14}, 10^{-13}, 10^{-12}, 10^{-11}, 10^{-10}, 10^{-9}, 10^{-8}, 10^{-7} M) were further dropped onto the surface of 6-MH-blocked cDNA/Au/**1**@PPY/GCE for 0, 30, 50, 70, 90 and 110 130 min to construct dsDNA/Au/**1**@PPY/GCE.

X-ray cystallography

Selecting a high-quality single-crystal of **1** and its diffraction intensity data were collected on a Bruker D8 venture photon II diffractometer with Mo Kα radiation (λ = 0.71073 Å) at 150 K. Direct methods were used to solve the structure of **1** and locate the heavy atoms, refined on F^2 by full-matrix least-squares method using the SHELXTL 97 program. Lorentz polarization and SADABS corrections were applied.[3–5] hydrogen atoms associated with water molecules were located from the difference Fourier map. All non-hydrogen atoms except for some Na, C, N, O and some water atoms were refined anisotropically. However, there are still solvent accessible voids accessible solvent voids in the check cif reports of crystal structures, suggesting that some lattice water molecules and counter cations should exist in the structures, which cannot be found from the weak residual electron peaks. Therefore, on the basis of elemental analysis and TG analysis, two $[H_2N(CH_3)_2]^+$ cations and sixty lattice water molecules are

directly added to the molecular formula. Crystallographic data and structure refinements for **1** are demonstrated in Table S1. Crystallographic data for **1** reported in this paper have been deposited in the Cambridge Crystallographic Data Centre with CCDC 2526761. These data can be obtained free of charge from the Cambridge Crystallographic Data Centre via www.ccdc. cam.ac.uk/data_request/cif

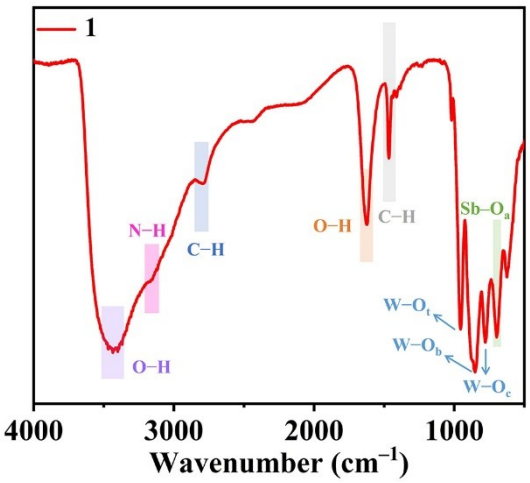

Fig. S1 The IR spectrum of **1**.

The IR spectrum of crystalline **1** has been measured using the solid sample palletized with KBr (Fig. S1). As we can see, it can be found that one very strong and wide absorption band at 3435−3401 cm^{-1} is because of the O–H stretching vibration. The weak absorption band appearing at 3172–3153 cm^{-1} and the weak absorption band at 2797−2775 cm^{-1} respectively correspond to the stretching vibrations of N–H and C–H bonds from $[H_2N(CH_3)_2]^+$ cations.[6] In the middle wavenumber region, one sharp absorption band at 1632−1625 cm^{-1} is derived from the O–H bending vibration from lattice and coordination water molecules while the weak band at 1465 cm^{-1} stem from the C–H band bending vibration of $[H_2N(CH_3)_2]^+$ cations.[7] Obviously, the IR spectrum of **1** shows the characteristic vibration bands originating from the trivacant Keggin $[SbW_9O_{33}]^{9-}$ fragments in the low wavenumber region (ν < 1000 cm^{-1}), which demonstrates four main typical vibration peaks from polyoxotungstate segments appearing at 956、852、778、698 cm^{-1}, which are separately attributed to the asymmetrical stretching vibrations of terminal W–O_t, corner-sharing W–O_b, edge-sharing W–O_c bands and Sb–O_a.[8,9]

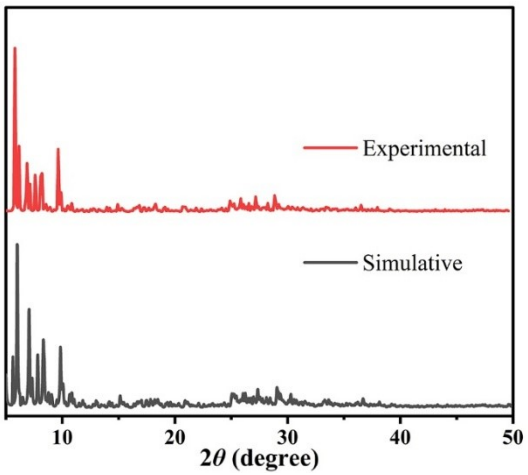

Fig. S2 Comparisons of experimental PXRD and the corresponding simulated XRD patterns of **1**.

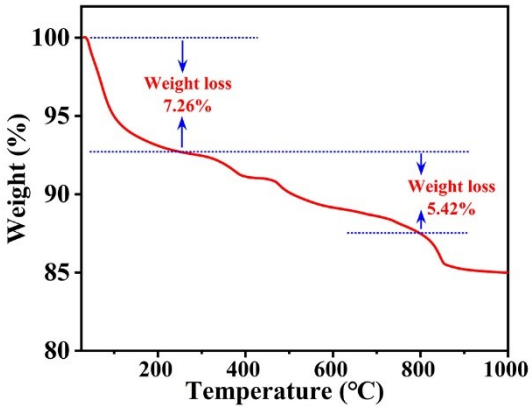

Fig. S3 The TG curve of **1**.

For the sake of exploring the thermal stability of **1**, the TG measurement was carried out from 25 to 1000 °C under a N_2 atmosphere at a heating rate of 10 °C min^{-1}. The TG curve suggests that **1** undergoes a three-step slow weight loss (Fig. S3). The first weight loss of 7.26% (calcd. 7.32%) in the temperature range of 25 to 250 °C, resulting from the release of eighty lattice water molecules. With temperature increasing from 250 to 800 °C, the second weight loss step of 5.42 % (calcd. 5.68 %), which is assigned to the removal of ten dimethylamine groups, the dehydration of eleven protons and twenty-six coordination water molecules. After the temperature exceeds 800 °C, the weight loss stem from the sublimation of WO_3.

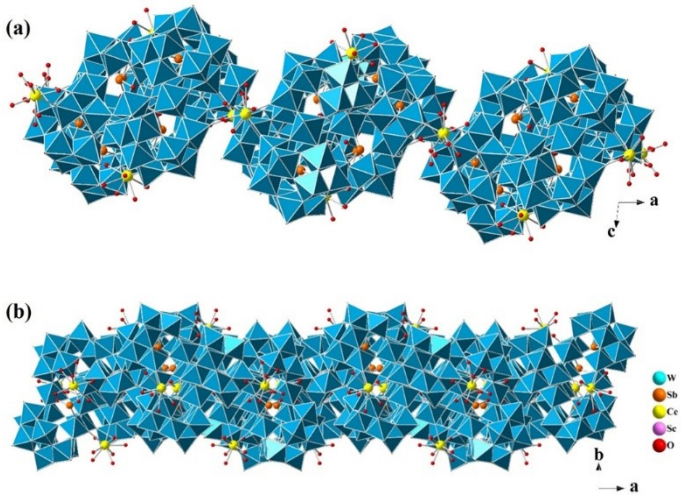

Fig. S4 (a) The 2-D layered **1** viewed along the *b*-axis. (b) The 2-D layered **1** viewed along the *c*-axis.

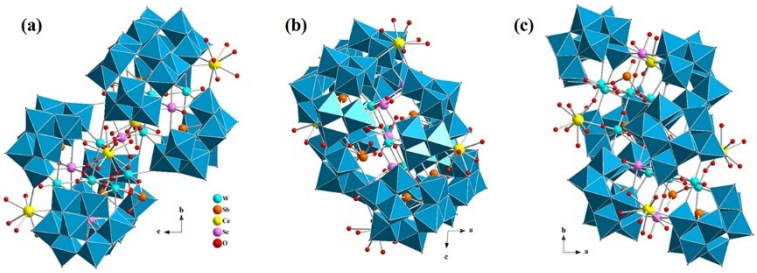

Fig. S5 (a) Structure of polyanion **1a** viewed along the *a*-axis. (b) Structure of polyanion **1a** viewed along the *b*-axis. (c) Structure of polyanion **1a** viewed along the *c*-axis.

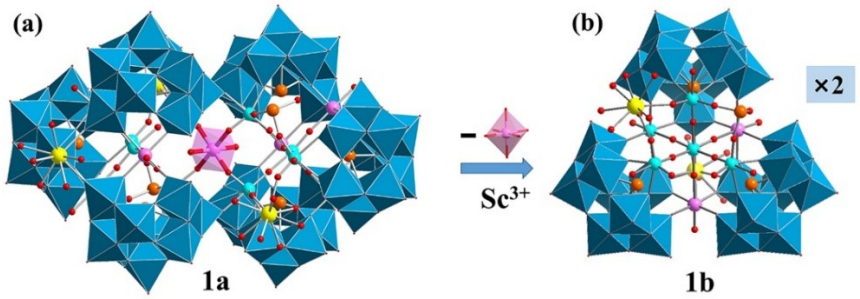

Fig. S6 The hexacoordinate Sc^{3+} cations serve as the symmetry center of **1a** to form two identical **1b**.

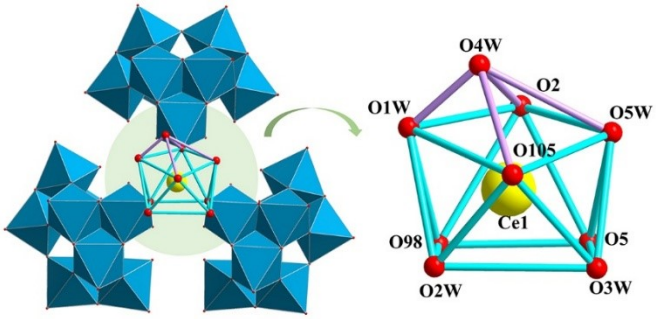

Fig. S7 The nine-coordinate monocapped square antiprismatic configuration of $Ce1^{3+}$ cation.

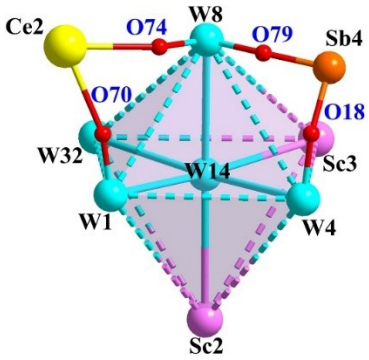

Fig. S8 Each of a Ce^{3+} and a Sb^{3+} cation is capped onto the octahedral $[Sc_2W_5O_{13}]^{10+}$ cluster through two oxygen atoms.

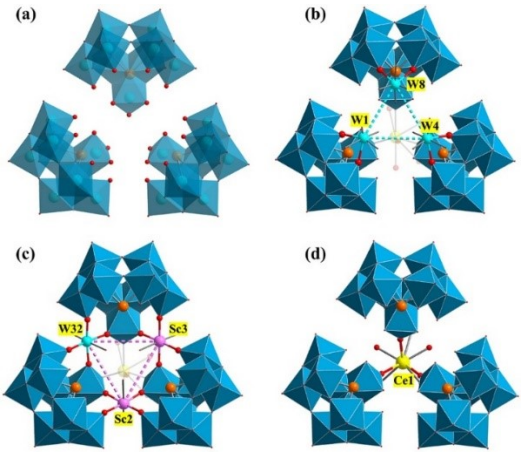

Fig. S9 (a) The vacancies in the three [B-*β*-SbW_9O_{33}]$^{9-}$ BBs in **1b** contain twenty-one highly reactive terminal oxygen sites. (b) The $W1^{VI}$, $W4^{VI}$ and $W8^{VI}$ centers each occupy two exposed sites of one [B-*β*-SbW_9O_{33}]$^{9-}$ BBs. (c) The $W32^{VI}$, $Sc2^{3+}$ and $Sc3^{3+}$ cations occupy 12 exposed sites of the three [B-*β*-SbW_9O_{33}]$^{9-}$ BBs. (d) The $Ce1^{3+}$ center occupies one exposed site of each [B-*β*-SbW_9O_{33}]$^{9-}$ BB.

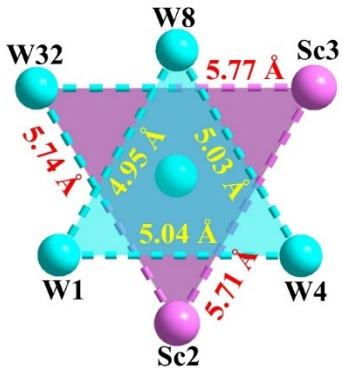

Fig. S10 These two triangular planes composed of W^{VI} centers and Sc^{3+} cations are staggered at an angle of 60°.

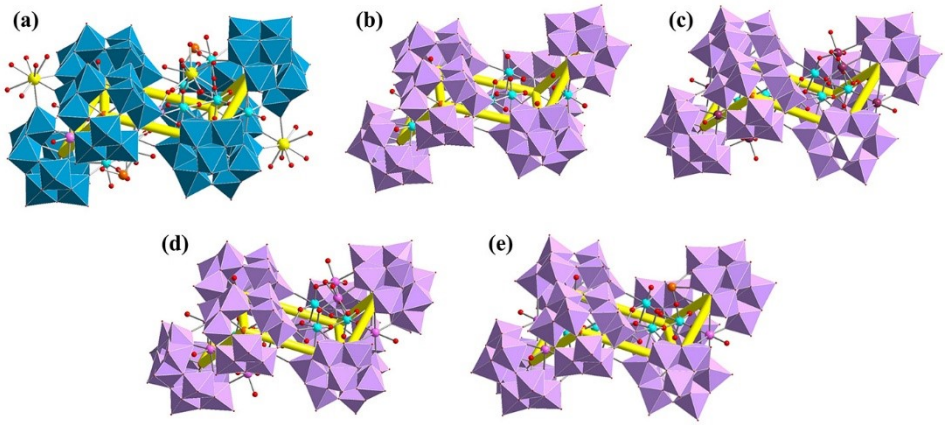

Fig. S11 (a) The chair-like conformation of **1a**. (b) The chair-like conformation of $[(B\text{-}\beta\text{-}SbW_9O_{33})_4(B\text{-}\alpha\text{-}SbW_9O_{33})_2(WO_2)_4(WO(H_2O))_6WO_5(H_2O)]^{26-}$. (c) The chair-like conformation of $[Fe_{11}(H_2O)_{14}(OH)_2(W_3O_{10})_2(B\text{-}\alpha\text{-}SbW_9O_{33})_6]^{27-}$. (d) The chair-like conformation of $[Sc_{11}W_6O_{20}(OH)_2(H_2O)_{16}(B\text{-}\beta\text{-}SbW_9O_{33})_6]^{27-}$. (e) The chair-like conformation of $[Sc_7Sb_2W_6O_{20}(H_2O)_8(B\text{-}\beta\text{-}SbW_9O_{33})_6]^{31-}$.

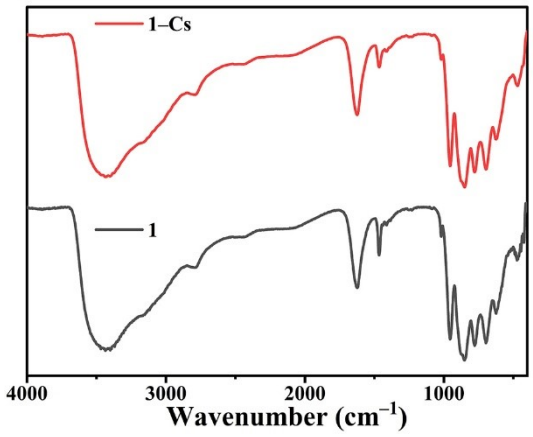

Fig. S12 IR spectra of **1–Cs** obtained from the aqueous solution of **1** by re-precipitating **1** with using CsCl.

The aqueous stability of **1** was verified via polyanion precipitation combined with IR spectroscopy (Fig. S12). Such excellent water stability enables the facile construction of the **1**@PPY film. The solution stability of **1** was further explored via a polyanion precipitation strategy, in which cesium chloride (CsCl) was introduced into the aqueous solution of **1** to induce polyanion precipitation. This methodology relies on a rational premise: if the polyanionic skeleton of **1** underwent hydrolytic decomposition into fragmented species in aqueous media, targeted

precipitation of the intact polyanion would be inhibited, and the resulting sediments would exhibit distinctly divergent IR fingerprint features. In this work, **1** was first dissolved in deionized water, followed by the introduction of excessive CsCl to afford the Cs-containing precipitate (**1**–Cs). As depicted in Fig. S12, the IR spectrum of the isolated **1**–Cs precipitate shows nearly perfect consistency with that of pristine solid **1**. Specifically, the diagnostic vibration bands of **1**–Cs at 948 cm^{-1} ($\nu W–O_t$), 898 cm^{-1} ($\nu W–O_b$), 784 cm^{-1} ($\nu W–O_c$), and 684 cm^{-1} ($\nu Sb–O$) closely match the characteristic absorption peaks of **1** at 956, 852, 778, and 698 cm^{-1}, respectively. These spectroscopic results unambiguously confirm the robust structural integrity of **1** in aqueous environments.

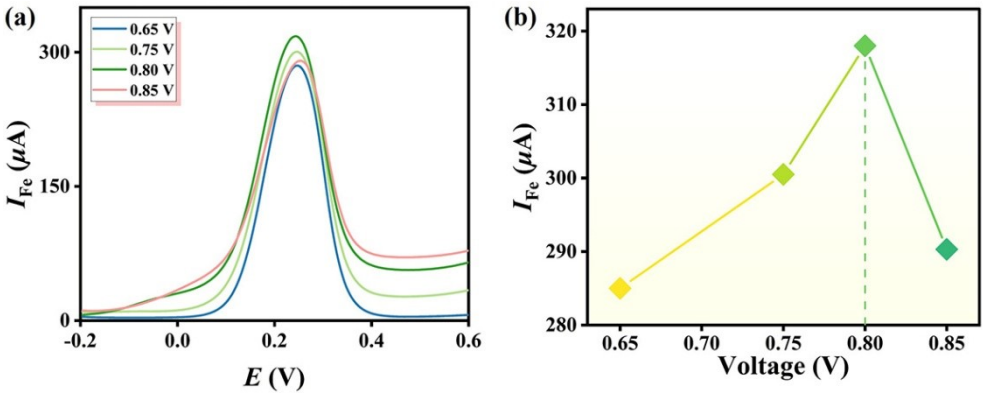

Fig. S13 (a) DPV curves and (b) I_{Fe} signal variations of different electropolymerization voltages (0.65, 0.75, 0.80 and 0.85 V). **1**: 50 mg·mL^{-1}, PY: 5 mM, and electropolymerization time: 50 s.

Electropolymerization voltage plays a critical role in determining the conductivity of the conductive polymer. To achieve the optimal **1**@PPY film, differential pulse voltammetry (DPV) was performed on **1**@PPY films fabricated at various applied voltages (0.65, 0.75, 0.80 and 0.85 V). As depicted in Fig. S13, the DPV peak current (I_{Fe}) rises sharply with increasing voltage from 0.65 V to 0.80 V, consistent with the progressive formation and enhanced structural integrity of the **1**@PPY film. In contrast, the I_{Fe} signal declines when the voltage exceeds 0.80 V. This can be ascribed to over-polymerization induced by excessively high voltage, leading to overly thick film deposition, severe agglomeration, and increased defects within the **1**@PPY film, thereby impairing its conductivity. Consequently, 0.80 V is chosen as the optimal electropolymerization voltage.

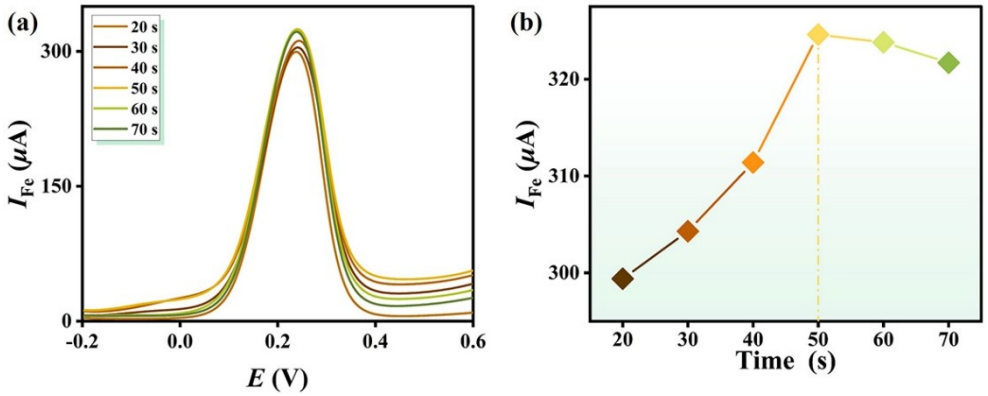

Fig. S14 (a) DPV curves and (b) I_{Fe} signal variations of different electropolymerization times (20, 30, 40, 50, 60 and 70 s).

We investigated the electropolymerization times (20, 30, 40, 50, 60 and 70 s) for the preparation of the **1**@PPY film (**1**: 50 mg·mL^{-1}, PY: 5 mM, and electropolymerization voltage: 0.8 V). As shown in Fig. S14, as the electropolymerization time increases from 0 to 50 s, the I_{Fe} signal rises rapidly, which is attributed to the gradual formation of a uniform and dense **1**@PPY film that facilitates interfacial electron transfer. However, when the electropolymerization time exceeds 50 s, the I_{Fe} signal gradually decreases, possibly because excessive polymerization leads to the formation of an overly thick and non-uniform **1**@PPY film. This increases the interfacial charge-transfer resistance, weakening the electrochemical response. Therefore, 50 s is determined as the optimal electropolymerization time for fabricating the **1**@PPY film.

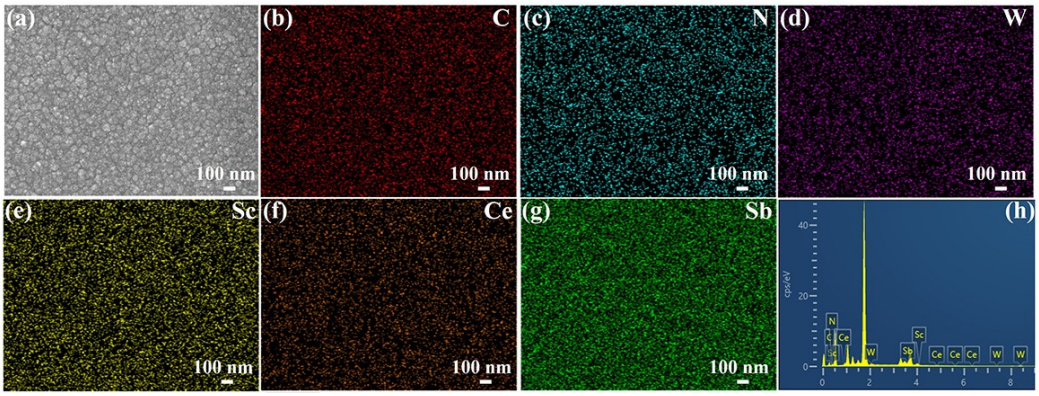

Fig. S15 (a) SEM image of **1**@PPY film. (b–g) SEM elemental mapping images of the **1**@PPY film with C, N, W, Sc, Ce, and Sb elements. (h) The SEM elemental mapping profile of the **1**@PPY film.

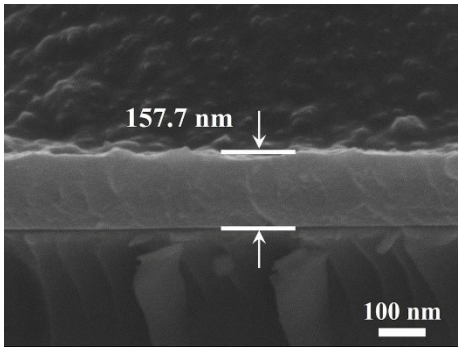

Fig. S16 The cross-sectional thickness of the **1**@PPY film (**1**: 50 mg·mL^{-1}, PY: 5 mM, electropolymerization voltage: 0.8 V, and electropolymerization time: 50 s).

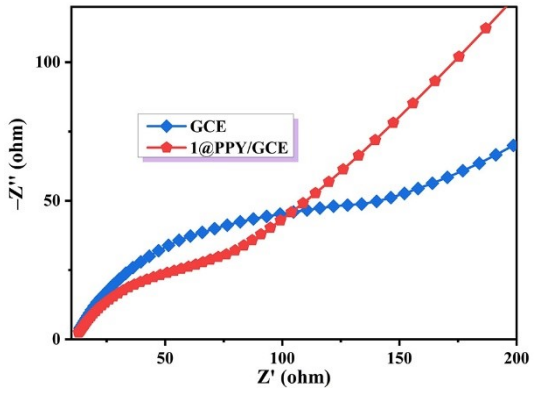

Fig. S17 EIS responses of the **1**@PPY/GCE and bare GCE.

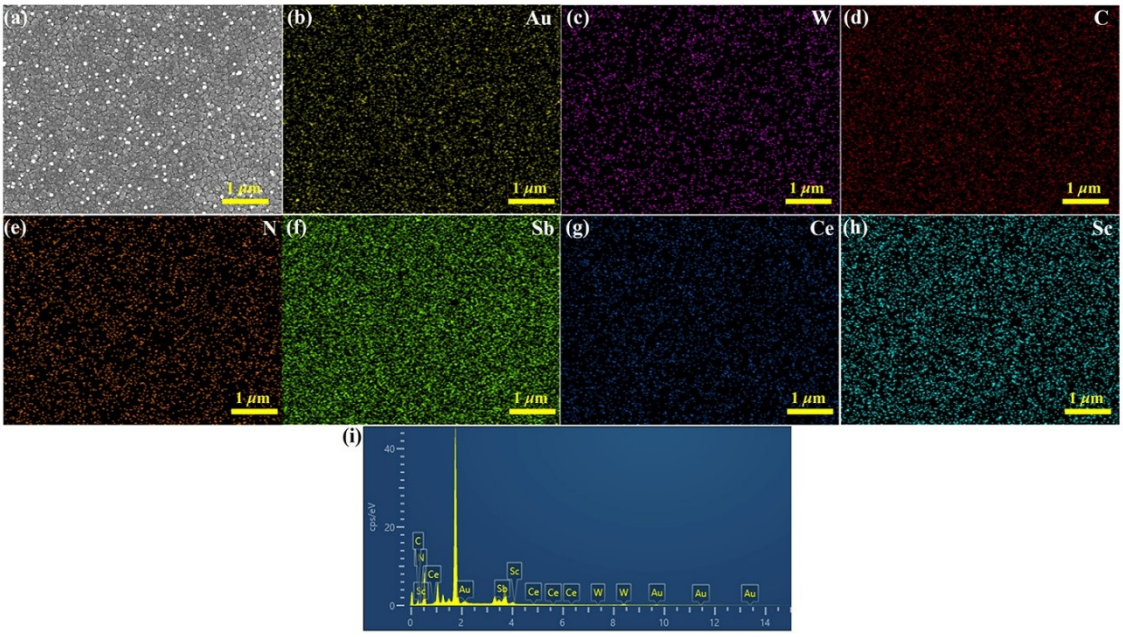

Fig. S18 (a) The SEM image of Au/**1**@PPY. (b–h) The SEM elemental mapping images of the Au/**1**@PPY film, corresponding to Au, W, C, N, Sb, Ce and Sc elements, respectively. (i) The SEM elemental mapping profile of the Au/**1**@PPY film.

We validated the successful deposition of Au NPs onto the **1**@PPY surface using SEM and SEM elemental mapping images. SEM image reveals a uniform distribution of Au NPs across the **1**@PPY film (Fig. S18a). The SEM elemental mapping images of the Au/**1**@PPY clearly reveal the coexistence of Au, W, C, N, Sb, Ce and Sc elements (Figure. S18b–i), providing compelling evidence for the successful modification of Au NPs onto the **1**@PPY/GCE.

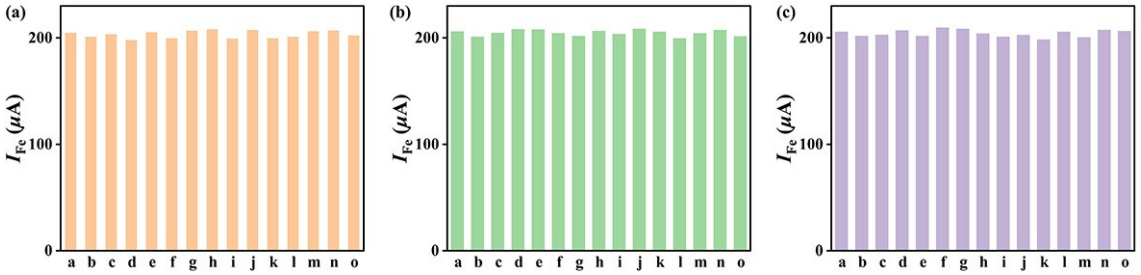

Fig. S19 (a) DPV current values (I_{Fe}) of the **1**-ECBS detecting CYFRA21-1 (10^{-10} M) co-existing with interfering DNA substances (10^{-9} M). (b) DPV current values (I_{Fe}) of the **1**-ECBS detecting CYFRA21-1 (10^{-10} M) co-existing with interfering DNA substances (10^{-8} M). (c) DPV current values (I_{Fe}) of the **1**-ECBS detecting CYFRA21-1 (10^{-10} M) co-existing with interfering DNA substances (10^{-7} M). a: CYFRA21-1, b: CYFRA21-1 + 1-mis-DNA, c: CYFRA21-1 + 2-mis-DNA, d: CYFRA21-1 + 3-mis-DNA, e: CYFRA21-1 + non-DNA, f: CYFRA21-1 + 1-mis-DNA + 2-mis-DNA, g: CYFRA21-1 + 1-mis-DNA + 3-mis-DNA, h: CYFRA21-1 + 1-mis-DNA + non-DNA, i: CYFRA21-1 + 2-mis-DNA + 3-mis-DNA, j: CYFRA21-1 + 2-mis-DNA + non-DNA, k: CYFRA21-1 + 3-mis-DNA + non-DNA, l: CYFRA21-1 + 1-mis-DNA + 2-mis-DNA + 3-mis-DNA, m: CYFRA21-1 + 1-mis-DNA + 2-mis-DNA + non-DNA; n: CYFRA21-1 + 2-mis-DNA + 3-mis-DNA + non-DNA; o: CYFRA21-1 + 1-mis-DNA + 2-mis-DNA + 3-mis-DNA + non-DNA.

Table S1. Crystallographic data and structure refinements for **1**.

Empirical formula	$C_{20}H_{303}Ce_4N_{10}Na_4O_{336}Sb_8Sc_5W_{64}$
Formula weight	19679.37
Crystal system	Monoclinic
Space group	*C*2/*c*
a, Å	34.5841(13)
b, Å	24.6662(8)
c, Å	38.2688(14)
α, deg	90
β, deg	95.6920(10)
γ, deg	90
V, Å^3	32485(2)
Z	4
μ, mm^{-1}	23.981
F(000)	34824
D_c, g cm^{-3}	4.024
T, K	139
Limiting indices	$-41 \le h \le 39$ $-29 \le k \le 28$ $-42 \le l \le 45$
Reflections collected	95560
Independent reflections	28348 [R_{int} = 0.0611]
Data/restrains/parameters	28348 / 25 / 1605
GOF on F^2	1.023
R_1, wR_2 ($I>2\sigma(I)$)	0.0651, 0.1456
R_1, wR_2 (all data)	0.0985, 0.1584

Table S2. Comparison of anodic peak current and electroactive surface area between **1**@PPY/GCE and GCE.

	Anodic peak current (I_p)	Electroactive surface area (A)
1@PPY/GCE	266.6 μA	0.166 cm^2
GCE	238.8 μA	0.144 cm^2

*Where I_p denotes the oxidation peak current, n is the number of transferred electrons (assumed to be 1.00), D is the diffusion coefficient (7.60 × 10^{-6} cm^2 s^{-1}), v is the scan rate (0.05 V s^{-1}), and C is the concentration of $[Fe(CN)_6]^{3-/4-}$ (10.0 mM). Based on the Randles–Sevcik equation: $I_p = 2.69 \times 10^5 n^{3/2} A D^{1/2} v^{1/2} C$, the electroactive surface area (A) of the **1**@PPY/GCE is calculated to be 0.166 cm^2, which is 1.17 times that of the bare GCE (0.144 cm^2).[10]

Table S3. Comparison of the sensitivity of different electrochemical sensors for monitoring tumor markers.

Detection methods	LOD (fM)	Linear range (M)	Ref.
Electrochemistry	2.14 fM	$1.0 \times 10^{-14} – 1.0 \times 10^{-6}$	11
Electrochemistry	10 fM	$1.0 \times 10^{-14} – 1.0 \times 10^{-7}$	12
Electrochemistry	178 fM	$1.0 \times 10^{-12} – 5.0 \times 10^{-11}$	13
Electrochemistry	59 fM	$1.0 \times 10^{-13} – 1.0 \times 10^{-9}$	14
Electrochemistry	8 fM	$1.0 \times 10^{-14} – 1.0 \times 10^{-8}$	15
Electrochemistry	1.37 fM	$1.0 \times 10^{-14} – 1.0 \times 10^{-7}$	This work

*The LOD was calculated according to the formula: $I_0 + 3\sigma = I = k \lg C_0 + b$ (I_0 denotes the baseline signal, determined as the average response of five blank measurements, σ represents the standard deviation of these five I_0 values, k and b correspond to the slope and intercept of the calibration equation, respectively; and C_0 is the LOD, Table S3).[8,16]

References:

1 M. Bösing, I. Loose, H. Pohlmann and B. Krebs, New strategies for the generation of large heteropolymetalate clusters: the *β*-B-SbW_9 fragment as a multifunctional unit, *Chem. Eur. J*., 1997, **3**, 1232–1237.

2 X. D. Jia, Z. G. Tang, L. N. Meng, Z. X. Wang, D. Wang, L. J. Chen and J. W. Zhao, Cerium-Encapsulated Sb^{III}–Se^{IV}-templating polyoxotungstate for electrochemically sensing human multidrug resistance gene segment, *Inorg. Chem*., 2023, **62**, 13639–13648.

3 G. M. Sheldrick, *SADABS: Program for Absorption Correction*; University of Göttingen: Göttingen, Germany, 1997.

4 G. M. Sheldrick, *SHELXL 97, Program for Crystal Structure Refinement*; University of Göttingen: Göttingen, Germany, 1997,

5 G. M. Sheldrick, *SHELXS 97, Program for Crystal Structure Solution*; University of Göttingen: Göttingen, Germany, 1997.

6 J. W. Zhao, C. M. Wang, J. Zhang, S. T. Zheng and G. Y. Yang, Combination of lacunary polyoxometalates and high-nuclear transition metal clusters under hydrothermal conditions: IX. A series of novel polyoxotungstates sandwiched by octa-copper clusters, *Chem. Eur. J*., 2008, **14**, 9223–9239.

7 S. S. Xie, D. Wang, Z. X. Wang, J. C. Liu, L. J. Chen and J. W. Zhao, Dual-heteroatom-templated lanthanoid-inserted heteropolyoxotungstates simultaneously comprising Dawson and Keggin subunits and their composite film applied for electrochemical immunosensing of auximone, *Inorg. Chem. Front.*, 2022, **9**, 350–362.

8 Z. G. Tang, J. X. Li, M. Wang, L. J. Chen and J. W. Zhao, Unraveling a Pr^{III}-bridged tetrahedral polyoxometalate constructed from $[SbW_{17}O_{59}]^{13-}$ units for logic gate programmed electrochemical biosensing of KRAS gene mutations, *Sens. Actuators B Chem.*, 2026, **454**, 139560.

9 Y. P. Li, Y. S. Dai, Z. G. Tang, L. J. Chen and J. W. Zhao, A Heterometallic decanuclear Ce^{III}–W^{VI} cluster incorporated antimonotungstate for sensitive electrochemical detection of multidrug resistance genes, *Inorg. Chem*., 2026, **65**, 4035−4045.

10 J. W. Li, H. L. Jin, M. Wei, W. J. Ren, J. S. Wang, Y. R. Zhang, L. G. Wu, B. S. He, Dual mode competitive electrochemical immunoassay for dibutyl phthalate detection based on PEI functionalized nitrogen doped graphene-$CoSe_2$/gold nanowires and thionine–Au@Pt core–shell, *Sens. Actuators B Chem*., 2021, **331**, 129401.

11 A. Jafari-Kashi, H. Rafiee-Pour and M. Shabani-Nooshabadi, A new strategy to design label-free electrochemical biosensor for ultrasensitive diagnosis of CYFRA 21–1 as a biomarker for detection of non-small cell lung cancer, *Chemosphere*, 2022, **301**, 134636.

12 M. Chen, Y. Y. Wang, H. L. Su, L, Mao, X, N. Jiang, T. Zhang and X. Z. Dai, Three-dimensional electrochemical DNA biosensor based on 3D graphene-Ag nanoparticles for sensitive detection of CYFRA21-1 in non-small cell lung cancer, *Sens. Actuators B Chem*., 2018, **255**, 2910–2918.

13 S. Y. Yang, L. Y. Zhao, X. Yang, L. Y. Yang, H. B. Fa, Y. Z. Wang, D. Q. Huo, C. J. Hou, D. D. Zhong and M. Yang, MBene as novel and effective electrochemical material used to enhance paper-based biosensor for point-of-care testing ctDNA from mice serum, *Chem. Eng. J*., 2024, **498**, 155345.

14 Z. Z. Xu, Z. G. Wang, D. M. Hu, H. Q. Chen, Y. F. Yan, Y. Li, M. J. Tu, Q. F. Shen, X. Y. Liu, R. Li, C. Lu, F. Xue, C. Y. Xie and G. Yang, MXene boosted ultrasensitive electrochemical detection of 5-hydroxymethylcytosine in genomic dna from complex backgrounds, *Adv. Funct. Mater*., 2024, **34**, 2313118.

15 L. L. Ma, L. Kang, Y. Z. Sun, J. W. Liu, H. X. Yang and M. S. Miao, Nitrogen-doped graphene quantum dots as electrochemiluminescence-emitting species for sensitive detection of KRAS G12C mutation via PET-RAFT, *Chem. Eur. J*., 2023, **29**, e202301602.

16 F. Jia, D. Liu, N. Dong, Y. Y. Li, S. Y. Meng, T. Y. You, Interaction between the functionalized probes: The depressed efficiency of dual-amplification strategy on ratiometric electrochemical aptasensor for aflatoxin B1. *Biosens. Bioelectron*., 2021, **182**, 113169.